

Article

Characteristics of Acoustic Emission Waveforms Induced by Hydraulic Fracturing of Coal under True Triaxial Stress in a Laboratory-Scale Experiment

Nan Li ^{1,2,*} , Liulin Fang ^{1,2}, Bingxiang Huang ^{1,2}, Peng Chen ^{1,2}, Chao Cai ^{1,3}, Yunpeng Zhang ^{1,2}, Xuan Liu ^{1,2}, Zhihuai Li ^{1,2}, Yaolin Wen ⁴ and Yanli Qin ^{1,2}

- ¹ State Key Laboratory of Coal Resources and Safe Mining, China University of Mining and Technology, Xuzhou 221116, China; ts19020006a31@cumt.edu.cn (L.F.); huangbingxiang@cumt.edu.cn (B.H.); ts20020007a31@cumt.edu.cn (P.C.); ts20120001a31@cumt.edu.cn (C.C.); TB20020041B4@cumt.edu.cn (Y.Z.); ts20020039a31tm@cumt.edu.cn (X.L.); ts20020130p21@cumt.edu.cn (Z.L.); 01190033@cumt.edu.cn (Y.Q.)
- ² School of Mines, China University of Mining and Technology, Xuzhou 221116, China
- ³ School of Safety Engineering, China University of Mining and Technology, Xuzhou 221116, China
- ⁴ School of Mathematics, China University of Mining and Technology, Xuzhou 221116, China; 10193791@cumt.edu.cn
- * Correspondence: linan@cumt.edu.cn

Abstract: Hydraulic fracturing (HF) is an effective technology to prevent and control coal dynamic disaster. The process of coal hydraulic fracturing (HF) induces a large number of microseismic/acoustic emission (MS/AE) waveforms. Understanding the characteristic of AE waveforms' parameters is essential for evaluating the fracturing effect and optimizing the HF strategy in coal formation. In this study, laboratory hydraulic fracturing under true triaxial stress was performed on a cubic coal sample combined with AE monitoring. The injection pressure curve and temporal variation of AE waveforms' parameters in different stages were analyzed in detail. The experimental results show that the characteristics of the AE waveforms' parameters well reflect the HF growth behavior in coal. The majority of AE waveforms' dominant frequency is distributed between 145 and 160 kHz during HF. The sharp decrease of the injection pressure curve and the sharp increase of the AE waveforms' amplitude show that the fracture already runs through the coal sample during the initial fracture stage. The "trapezoidal" rise pattern of cumulative energy and most AE waveforms with low amplitude may indicate the stage of liquid storage space expansion. The largest proportion of AE waveforms' energy and higher overall level of AE waveforms' amplitude occur during the secondary fracture stage, which indicates the most severe degree of coal fracture and complex activity of internal fracture. The phenomenon shows the difference in fracture mechanism between the initial and secondary fracture stage. We propose a window-number index of AE waveforms for better response to hydraulic fracture, which can improve the accuracy of the HF process division.

Keywords: coal; true triaxial stress; hydraulic fracturing; acoustic emission; waveform characteristics; statistics analyze



Citation: Li, N.; Fang, L.; Huang, B.; Chen, P.; Cai, C.; Zhang, Y.; Liu, X.; Li, Z.; Wen, Y.; Qin, Y. Characteristics of Acoustic Emission Waveforms Induced by Hydraulic Fracturing of Coal under True Triaxial Stress in a Laboratory-Scale Experiment. *Minerals* **2022**, *12*, 104. <https://doi.org/10.3390/min12010104>

Academic Editor: Yosoon Choi

Received: 1 December 2021

Accepted: 9 January 2022

Published: 16 January 2022

Publisher's Note: MDPI stays neutral with regard to jurisdictional claims in published maps and institutional affiliations.



Copyright: © 2022 by the authors. Licensee MDPI, Basel, Switzerland. This article is an open access article distributed under the terms and conditions of the Creative Commons Attribution (CC BY) license (<https://creativecommons.org/licenses/by/4.0/>).

1. Introduction

Hydraulic fracturing (HF) is a widely used rock failure and reservoir modification technology [1–3]. In recent years, HF has been widely used in preventing and controlling coal dynamic disaster, such as rock burst, coal, and gas outburst, which have achieved good results [4–6]. Under high-pressure fluid, a fracture occurs in coal and rock mass, and a hydraulic fracture network structure is formed. Many studies show that rock materials will release energy in the form of elastic waves in the process of deformation and failure. Microseismic (MS) monitoring/acoustic emission (AE) monitoring technology can continuously collect the elastic waveform generated in rock deformation and failure in real-time. The

biggest difference between MS monitoring and AE monitoring is the frequency range of monitoring. The frequency range of MS monitoring is generally distributed in 10–1000 Hz, while the general monitoring range of AE monitoring system is 20 kHz–20 MHz. Acoustic emission monitoring systems are generally used in laboratory physical simulation tests to monitor coal rock fractures. It can be used to study the internal structure and stability of rock mass, crack propagation mechanism, and distribution pattern of crack. The results show that the MS/AE waveform produced by rock failure under high-pressure fluid has significant characteristics [6–8]. As a special kind of rock, coal has the characteristics of the soft structure, developed joints and fissures, and strong heterogeneity. In addition, most of the coal is in the state of three-dimensional stress during HF in-field application. Therefore, it is thought to be of great significance to carry out AE monitoring experiments of true triaxial HF of coal samples and systematically study AE waveform characteristics of coal samples in different stages of true triaxial HF for AE monitoring and the evaluation of coal HF and further understanding of the fracture propagation mechanism of coal HF at the field scale.

Some scholars have carried out many experimental and theoretical research on AE monitoring of different coal and rock failure and obtained a series of research results. They have systematically studied the characteristics and the variation law of AE waveform parameters, such as dominant frequency, count, and energy. Furthermore, they also have achieved a series of results of statistical parameters of different coal and rock under different loading modes [9–39]. Some scholars have researched AE monitoring of rock HF. AE monitoring experiments of sandstone, shale, and other brittle rocks have been carried out in the laboratory. Moreover, the variation law of the AE count, energy, event number, and other statistical parameters in rock HF and their corresponding relationships with the hydraulic pressure curve have been analyzed. Based on the AE location, the temporal and spatial propagation process and distribution pattern of hydraulic fractures were studied, and the initiation and propagation mechanism of the hydraulic fracture was explored by using the AE focal mechanism [40–50]. In addition, some scholars also began to use AE monitoring to study coal HF and tested and analyzed the time variation characteristics of AE events, energy, and other statistical parameters generated in coal HF. Meanwhile, some have preliminarily studied AE localization and temporal–spatial evolution distribution law of coal HF [51–54]. Therefore, the current research mainly focuses on the variation of AE statistical parameters in HF of coal and rock materials, as well as the propagation mechanism and spatial and temporal distribution of HF based on AE localization.

An AE waveform generated by coal rock failure contains an abundant rupture source and medium information. Zhang et al. [55] put forward the characteristic parameter of dominant frequency to secondary dominant frequency (F). The research shows that the numbers of the dominant frequency and secondary dominant frequency bands of AE increase first and then decrease in the rupture process of saturated granite. He et al. [56] showed that, with the increase of load, the frequency changes from a low value to high value, the band of frequency becomes wider and wider, and the shape of wave changes from unimodal to multimodal. Pu et al. [57] found that the flow of high-pressure magmatic fluid in rock fractures can produce unique seismic waveforms like screws and single water drops when studying the waveform of a Datun Volcano earthquake. Li et al. [58] and Li et al. [59] showed that the amplitude–frequency characteristics of vibration wave signals induced by HF of coal seams in underground coal mines are significantly different from those induced by mining activities and shale HF. Tang et al. [60] showed that the amplitude change rate of AE waveform induced by shale HF can be used as an index to judge fracture initiation and propagation. Liang et al. [61] showed that the frequency and RA value, which is the rise time over the amplitude of the AE waveform, can qualitatively evaluate the fracture mechanism of coal and rock.

An accurate evaluation of the influence range of HF in coal seam is one of the most difficult problems in the world. Hydraulic fracture propagation is affected by ground stress, coal, and rock properties and the water injection rate in engineering practice. At

present, time–frequency analysis techniques of MS analysis mainly focus on the dynamic process of fracture propagation. However, due to the complicated occurrence conditions of deep-buried coal seams, the sensor response and waveform recording results are different, which causes the time spectrum of waveform become more complex. At this time, if only a single time–frequency analysis method is used to analyze the dynamic propagation characteristics of hydraulic fracture, the accuracy and reliability of the analysis results will be greatly reduced. Therefore, it is necessary to synthesize various time–frequency analysis methods and analyze the temporal variation characteristics of AE waveforms' parameters, which can provide a theoretical basis for qualitatively analysis of the fracture propagation features during the whole process of HF.

This study aimed to reveal the characteristics of the dynamic growth process of hydraulic fracture in coal through the analysis of the AE monitoring data. The cubic coal samples of a synchronous AE monitoring experiment under a true triaxial HF experiment were taken as an example for the real-time interpretation of AE features to further obtain detailed insights on HF. The entire process was initially divided into several sub-stages according to the injection pressure curve and water injection flow. An AE waveforms' parameters automatic picking batch processing program was designed based on the traditional time–frequency analysis method. The temporal variation characteristics of AE waveforms' parameters were then analyzed. Moreover, a window-number index was proposed to optimize the stage division of HF based on the acquired knowledge of the AE response features during laboratory HF. The analysis results provided us a reference for understanding the dynamics of hydraulic fracture through AE monitoring and further interpretation of the recorded microseismic monitoring field data, which provides guidance for coal dynamic disaster prevention and control.

2. Experimental Program

2.1. Coal Sample Preparation

In this study, the coal samples were selected from Xiezhuang Coal Mine in Shandong. The coal sample was processed into three-cylinder samples of $\Phi 50 \text{ mm} \times 100 \text{ mm}$ and three cubic samples of $150 \text{ mm} \times 150 \text{ mm} \times 150 \text{ mm}$, while the cylinder samples were used to test the uniaxial compressive strength (UCS), and the cubic samples were made for the true triaxial HF experiment. After this, the samples' surfaces were polished smooth, and the maximum non-parallelism of the two ends did not exceed 0.05 mm. Finally, a fracturing hole was drilled vertically at the center of the surface of the cube coal sample. The hole was 90 mm in depth and 14 mm in diameter. The hole-sealing device was fixed and sealed in the fracturing hole by using planting glue. The packing depth of the hole-sealing device was 60 mm, and the remaining 30-mm open hole section was used for fracturing.

2.2. Laboratory Equipment

We developed a true triaxial HF loading system for coal rock with AE monitoring. As Figure 1 shows, the system mainly includes a true triaxial test bench, HF system, and AE monitoring system. The true triaxial experiment bench mainly includes the main loading frame, vertical loading module, triaxial loading chamber, computer control module, data acquisition and processing software module, and other parts. The testing machine uses programmable electrohydraulic servo control in both the vertical and horizontal directions, and the control software can realize complex three-way stress paths to be loaded. The HF system uses a MOOG valve and oil–water conversion booster to achieve hydraulic pressure control loading, and the hydraulic pressure can reach up to 63 MPa. Water can be injected according to the flow control (L/min) or pressure control (MPa/min). Among them, the water injection rate can be arbitrarily selected between 0 and 1000 mL/min. During the process of HF, the water injection rate, cumulative injection volume, real-time water pressure, and other such data can be collected in real-time. Through the control software system, dynamic adjustment of the fracturing parameters can be achieved. The AE monitoring system comprises AE sensors, preamplifiers, PCI-Express AE acquisition

cards, and AEwin monitoring software (1.30, MISTRAS Group, Inc., 195 Clarksville Road Princeton Junction, USA). It can realize the AE parameter setting, AE statistical parameters, AE waveform synchronous acquisition and analysis, and other functions. Our large number of tests performed during the early stage of the laboratory showed that the frequency of coal and rock mass fracture signal is distributed in the low-frequency band. Some scholars have carried out in-depth research on the fracture frequency of coal and rock mass and concluded that the frequency band of fracture frequency is mainly distributed in 0–200 kHz [61–65]. Therefore, in this experiment, the AE monitoring system uses a sampling rate of 500 kHz resulting in a Nyquist frequency equal to 250 kHz. The sampling length is 2048 points, the preamplifier gain is 40 dB, and the trigger threshold is 40 dB.

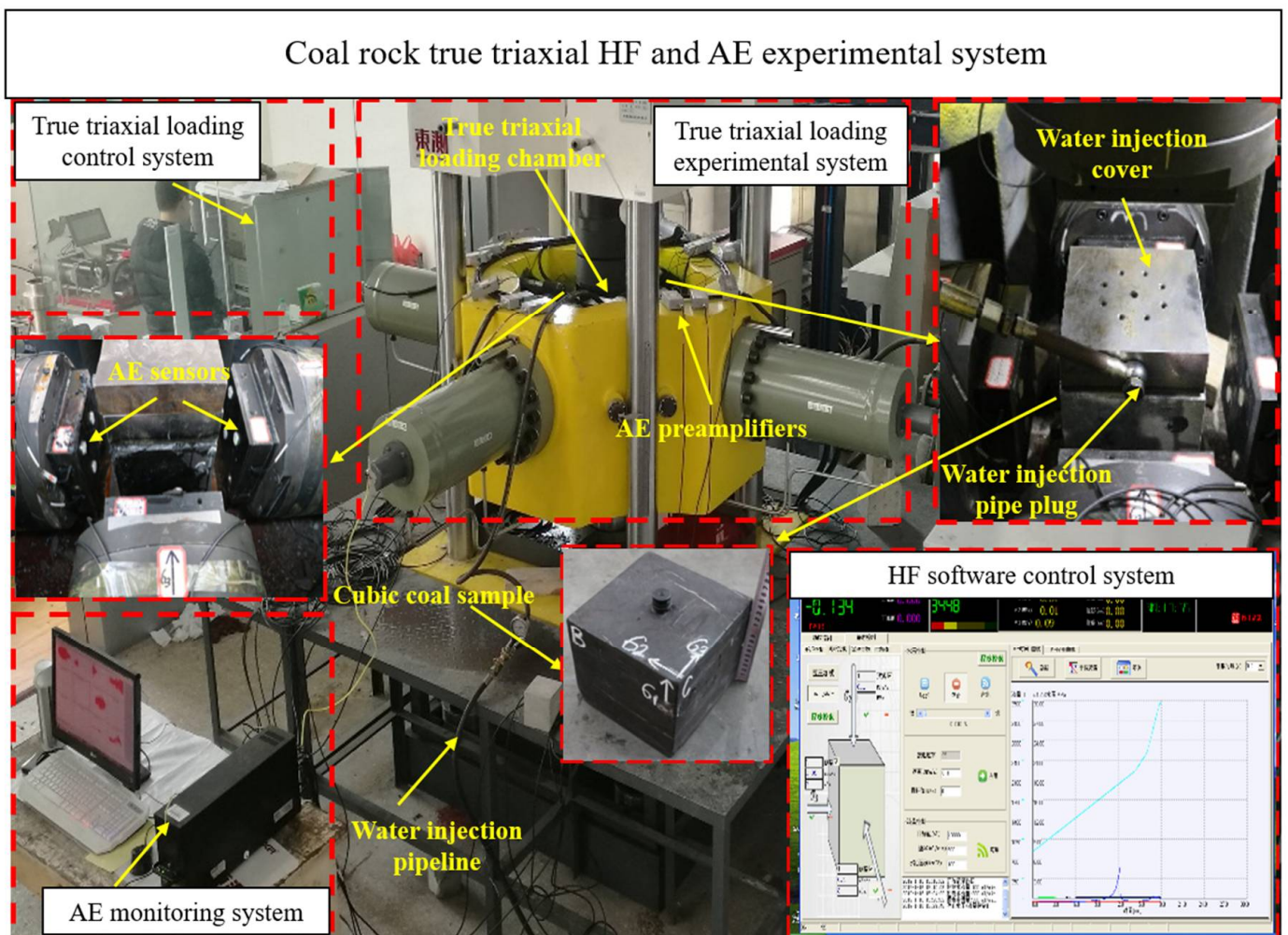


Figure 1. Coal rock true triaxial HF and AE experimental system.

2.3. Experiment Process

We used the MTS testing system to carry out the UCS of three-cylinder samples. The uniaxial compression experiment adopted stress loading pattern with the loading rate in 0.5 MPa/s for the duration of the process. The UCS of the coal sample was 13.32 MPa. Based on the results of the UCS of cylinder coal sample, the maximum principal stress of true triaxial loading was set to 12 MPa, the intermediate principal stress was set to 8 MPa, and the minimum principal stress was set to 4 MPa, respectively. The loading rate was 0.02 MPa/s. According to the characteristics of acoustic emission waveform produced by the deformation and failure of coal samples, 12 R15 AE sensors were used in this study with an acceptance frequency range of 50 kHz~400 kHz. As shown in Figure 2, the AE sensors are respectively arranged on 4 vertical surfaces of the cube with 3 on each vertical

surface. In order to ensure the reliability of the AE waveform data, the sensor must always be in direct contact with the coal sample. Figure 3 shows the flow chart of this experiment, and the specific practical steps are as follows:

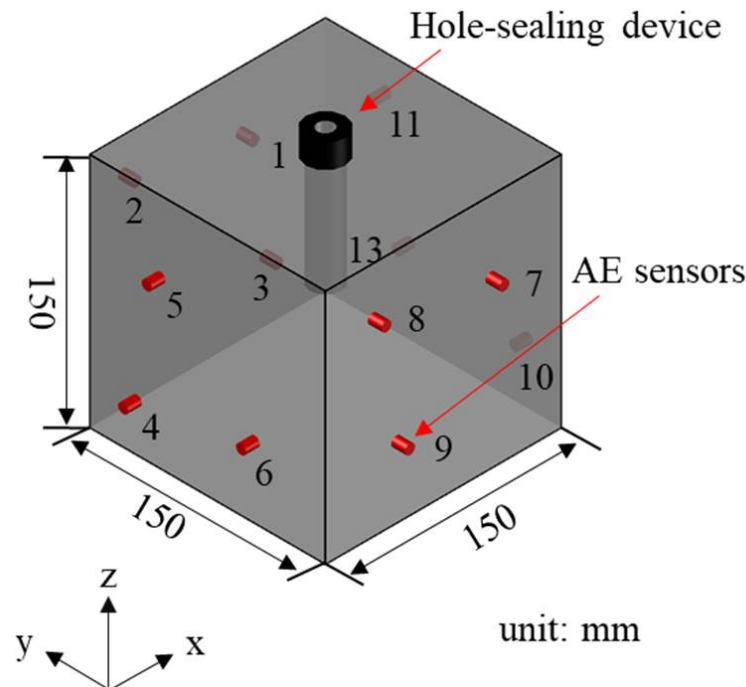


Figure 2. The layout of the AE sensors.

(1) According to mechanical parameters, such as uniaxial compressive strength of coal samples determined true triaxial loading parameters such as three-dimensional pressure level, loading mode, and rate in three directions.

(2) According to monitoring needs, determine a reasonable arrangement of AE sensors. Install the sensor in a removable loading block and apply couplant on the surface of the sensor.

(3) Butter was applied evenly to the coal sample and loading block surface to reduce the end friction effect. Cut a round hole at the corresponding antifriction plate position to make the AE sensor directly contact the surface of the coal sample.

(4) Put the coal sample into the true triaxial loading chamber. Then, connect one end of the HF pipeline to the fracturing cover plate and the other end to the HF system. After the HF pipeline is connected, use a hand pump for the airtightness test.

(5) Reasonable setting of AE monitoring parameters. Before the start of the experiment, do lead break tests to test the coupling quality of the sensor and the accuracy of the monitoring system.

(6) After the debugging of all equipment, according to the set loading path, the true triaxial loading is carried out. When all three-dimensional pressures are loaded to the set value, the constant load is maintained.

(7) After constant load for a period, the coal sample no longer produces AE waveforms basically. According to the set water injection rate, water injection and fracturing are performed until the coal sample is destroyed.

(8) During the experiment, the AE waveforms generated are collected synchronously, and the experimental phenomena are recorded in real-time.

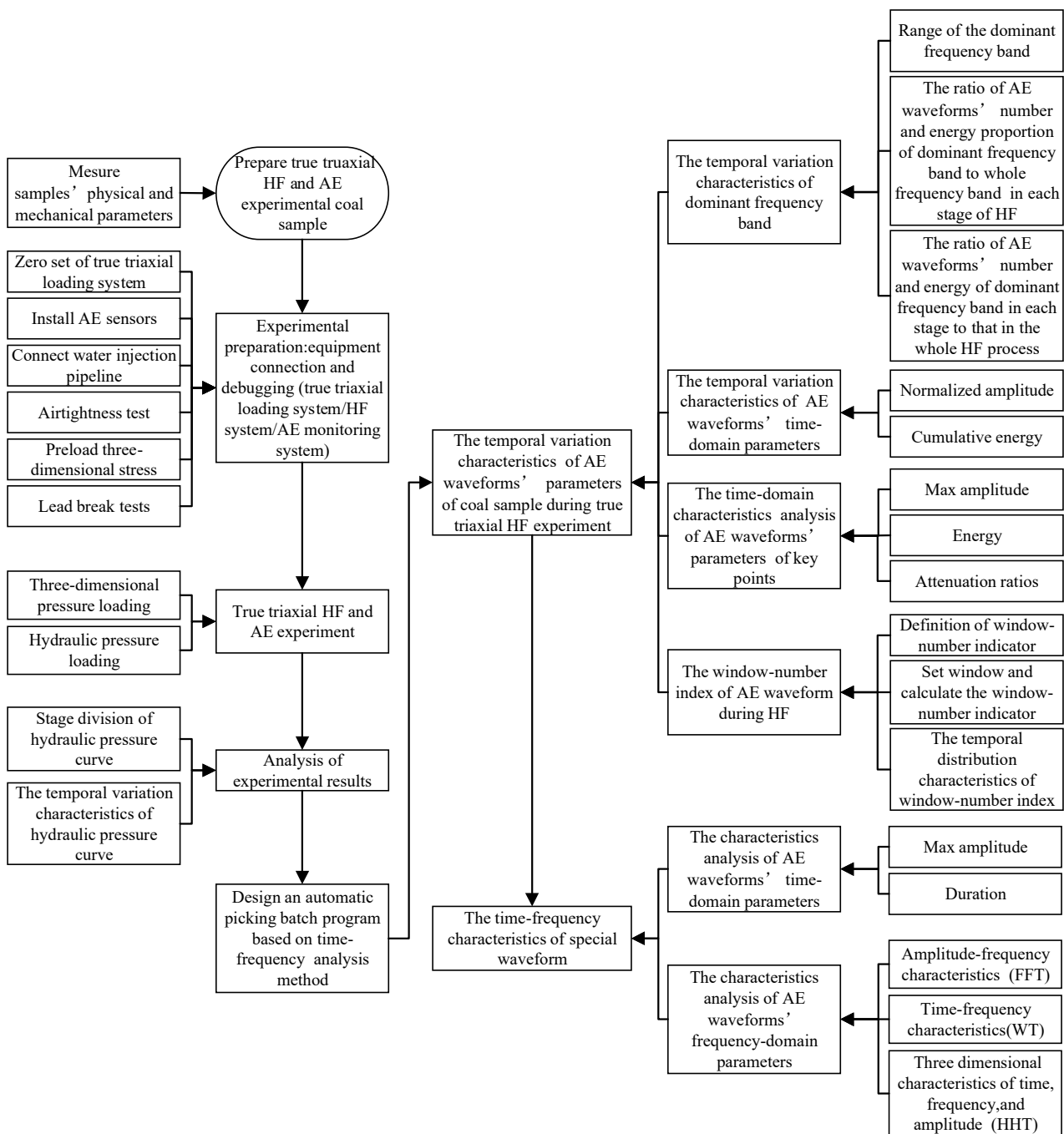


Figure 3. Flow chart of true triaxial HF and AE monitoring experiment for coal samples.

3. Experimental Results and Analysis of True Triaxial HF

Based on the above experimental method, we performed true triaxial HF experiments on the coal samples combined with AE monitoring. As shown in Figure 4, the whole loading process lasts 2420 s, with the three-dimensional pressure loading stage lasting 540 s. The three-dimensional pressure remains constant when it reaches 12 MPa, 8 MPa, and 4 MPa. In order to keep the overall acoustic emission waveform response at a lower level, hydraulic loading was started after an interval of 90 s after the three-dimensional pressure loading stage. As a result, the hydraulic pressure process lasted 1790 s. During the period from 630 s to 1915 s, the water injection rate was controlled at 100 mL/min. The water injection rate was adjusted to 200 mL/min during the period from 1915 s to 2420 s.

The duration of the whole experimental process and the hydraulic pressure parameters are shown in Table 1.

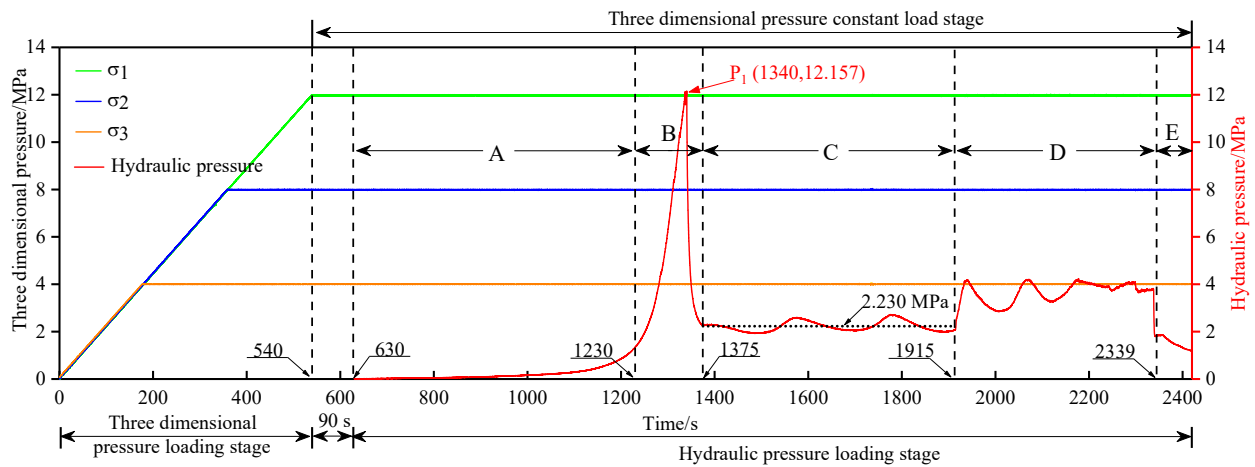


Figure 4. Hydraulic pressure curve and three-dimensional pressure curve during HF experiment.

Table 1. Parameters of true triaxial HF experimental system.

Three-Dimensional Pressure $\sigma_1/\sigma_2/\sigma_3$	Duration/s	Hydraulic Pressure Duration/s	Final Constant Load Time of Three-Dimensional Pressure /s	Peak Time of Hydraulic Pressure /s	Peak Hydraulic Pressure/MPa
12/8/4	2420	1790	540	1340	12.157

We combined the characteristics of hydraulic pressure curve, the change of water injection flow, and related experimental phenomenon. The hydraulic pressure loading was divided into five stages according to the time sequence. The details are shown in Figure 4.

Stage A (630–1230 s): It is the pressure-building stage. Water entered the fracturing borehole through the water injection pipeline and the hole packer. It gradually filled the bare hole section at the bottom of the borehole. With the increase of water injection, hydraulic pressure began to rise slowly.

Stage B (1230–1375 s): It is the initial fracture stage. The hydraulic pressure continued to increase. At 1340 s, the hydraulic pressure reached the peak point P1, and the hydraulic pressure value was 12.1570 MPa. Subsequently, the hydraulic pressure decreased sharply. At 1375 s, the hydraulic pressure decreased to 2.278 MPa. Meanwhile, we observed the true triaxial loading chamber and found that water flowed out from the bottom of the apparatus, so we judged that the coal body was ruptured. High-pressure water had more effect on the coal body in this process.

Stage C (1375–1915 s): It is a liquid storage space expansion stage. After a crack of the coal body, the hydraulic pressure drops to a low level. At this time, not the water pressure but the water erosion played a leading role in weakening the coal body. Moreover, the main crack of the coal body is closed under three-dimensional pressure loading, and there was a small liquid storage space inside the coal sample. As the injection rate kept constant, the liquid storage space was full of water, and hydraulic pressure continued to rise to a critical value. Then, the liquid storage space was expanded, and the hydraulic pressure decreased until the water filled the space once again. The hydraulic pressure curve showed a cyclic rise and fall. Along the initial crack initiation path, the liquid storage space in the coal body gradually expands from the bare hole section to the coal sample surface during the stage C. The fluctuation of the hydraulic pressure curve is shown in Figure 4, with the maximum hydraulic pressure of 2.724 and the average fluctuation of 2.230 MPa.

Stage D (1915–2339 s): It is the secondary fracture stage. At 1915 s, we changed the water injection rate from 100 mL/min to 200 mL/min, while the hydraulic pressure value was 2.109 MPa. At the same time, the hydraulic pressure increased from 2.109 MPa to 4.1550 MPa sharply, which means that water filled the initial through crack. Then, the hydraulic pressure of early-stage D appeared similar to the periodic rise and fall in stage C. However, the average value of hydraulic pressure in stage D was higher than that of stage C, and the water flowed out from the bottom of the apparatus again. During end-stage D, the hydraulic pressure curve showed a more irregular waveform than before. The hydraulic pressure plummeted from 3.788 MPa to 1.79 MPa at 2339 s. Therefore, we judged that the secondary rupture of the coal body occurred at this moment.

Stage E (2339–2420 s): It is the last stage of HF. The water injection rate was kept at 200 mL/min. This moment, the three-dimensional pressure cannot make the through crack close, and water continued to flow out from the bottom of the apparatus. The hydraulic pressure curve gradually decreased. Therefore, the coal body was judged to be a complete failure.

4. Temporal Variation Characteristics of AE Waveforms' Parameters

4.1. The Temporal Variation Characteristics of AE Waveforms' Dominant Frequency and Energy

The AE waveform dominant frequency and energy are frequently used AE characteristics parameters. They are widely used to study coal rock crack regularity. During rock failure under loading, the AE signal generated is essentially a discrete random signal, and its frequency will change over time [10,27,33,39,61–65]. Fast Fourier Transform (FFT) is a standard waveform analysis algorithm. This algorithm can provide the amplitude and frequency information evolution processes. Waveform energy can directly reflect the size of the event energy level and indirectly reflect the size of the internal coal crack during this period. On this basis, we combine the temporal variation characteristics of AE parameters with the loading process of coal samples, analyzing the distribution characteristics of the dominant frequency and the regularity of the energy proportion of the corresponding dominant frequency.

Figure 5a draws the original waveform, and Figure 5b shows the two-dimensional spectrum after FFT. As shown in Figure 5b, the dominant frequency of the waveform is a multipeak structure, and the peak frequency is 43.21 kHz. At present, some scholars have analyzed the evolution characteristics of the AE frequency spectrum in rock fracture from the perspective of the primary–secondary frequency ratio [36,55,66].

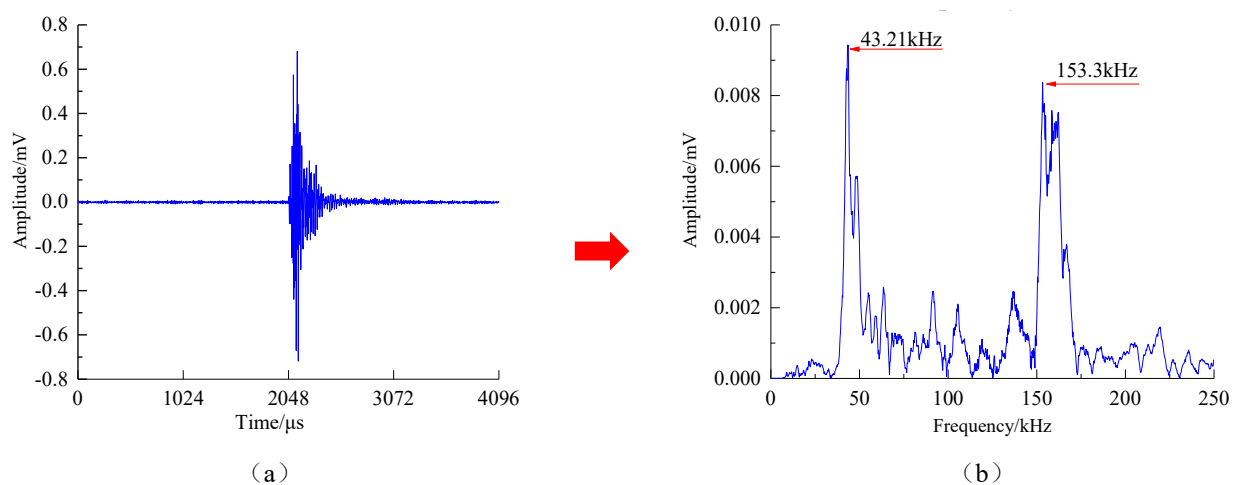


Figure 5. Waveform time–domain and frequency–domain diagram ((a) original waveform diagram and (b) amplitude–frequency diagram).

In this section, we combined FFT with a batch processing program, and the dominant frequency of the AE waveform during the true triaxial HF can be picked up in a batch. Based on this, ignoring the influence of multipeak frequency, the distribution regularity and evolution characteristics of the dominant frequency in the HF are studied.

As shown in Figure 6, the distribution range of the AE waveform dominant frequency is 30–270 kHz. We found that the majority of the dominant frequency is distributed between 145 and 160 kHz. For the details, the waveform number in this frequency band to the whole frequency band ratio is up to 83.97%, and the proportion of its energy is up to 87.28%. As shown in Table 2, the number and energy proportion of these frequency band waveforms in each stage of HF are more than 65%. This frequency band is defined as the dominant frequency band of the whole band. Therefore, we replace the whole band with dominant frequency band to study the temporal variation characteristics of the dominant frequency. It can be seen from Table 3 for the waveform number and energy of the dominant frequency band in each stage to that in the whole HF process ratio.

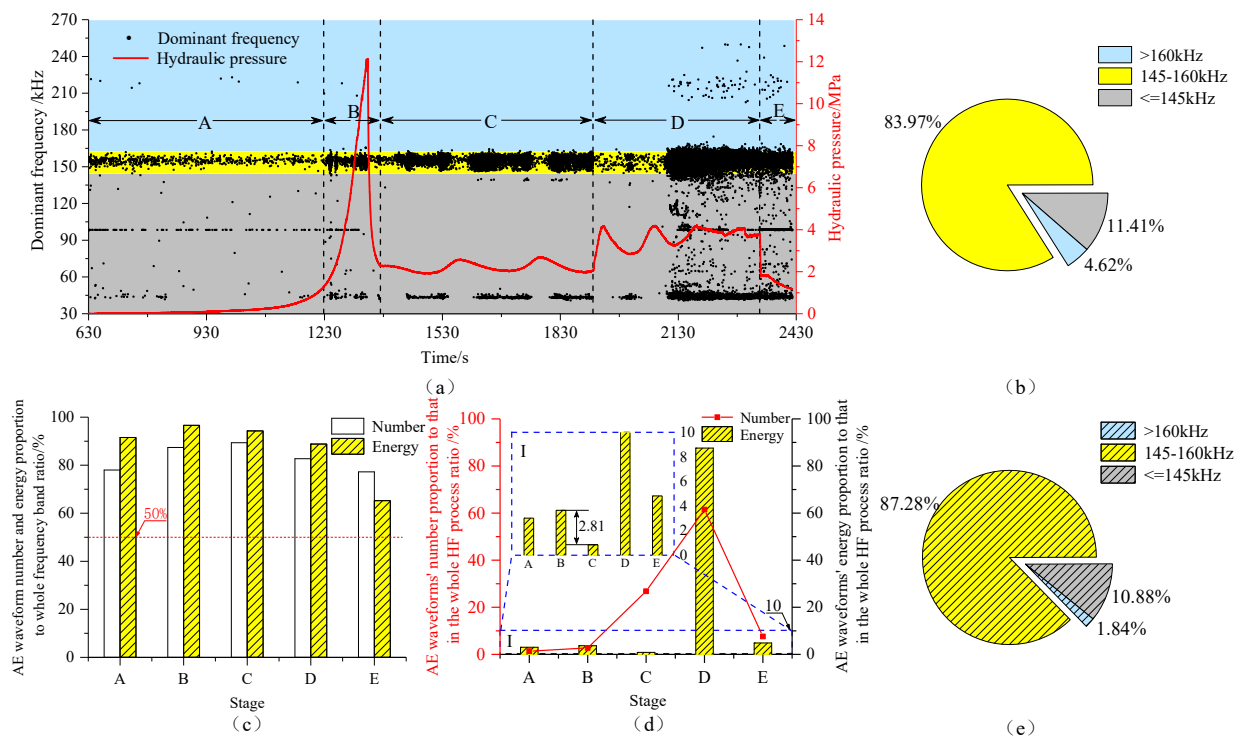


Figure 6. AE waveform dominant frequency distribution during true triaxial HF and characteristics of the AE waveforms’ parameters (number and energy) proportion in the dominant frequency band ((a) AE waveform dominant frequency distribution in the true triaxial HF, (b) AE waveforms’ number proportion of the dominant frequency band to the whole frequency band ratio, (c) AE waveforms’ number and energy proportions of the dominant frequency band to the whole frequency band ratio in each stage of HF, (d) AE waveforms’ number and energy of the dominant frequency band in each stage to that in the whole HF process ratio, and (e) AE waveforms’ energy proportion of dominant frequency band to the whole frequency band ratio).

Table 2. The ratio of AE waveforms’ numbers and energy proportions of the dominant frequency band to the whole frequency band in each stage of HF.

Dominant Frequency Band to Whole Frequency Band Ratio/%	Each Stage of HF	A	B	C	D	E
	Number		78.58	87.54	89.36	84.01
Energy		91.55	96.59	94.29	88.82	65.26

Table 3. The ratio of waveforms' numbers and energy of the dominant frequency bands in each stage to that in the whole HF process.

Each Stage to Whole HF Ratio/%	Each Stage of HF	A	B	C	D	E	Total
	Number		1.37	2.74	26.79	61.49	7.61
Energy		3.03	3.67	0.86	87.60	4.84	100

As shown in Figure 6d, the number proportion of the dominant frequency band waveform in each stage of HF generally increases first and then decreases and reaches the maximum value of 61.49% in stage D. In the whole process of HF, the waveform energy of the dominant frequency band in D stage accounts for 87.60%, and its proportion in other stages is less than 10%. In general, the number and energy of the waveform in stage D to that in whole process ratio are both the largest. This indicates that, in stage D, the internal rupture degree of the coal body is the most severe. According to the previous analysis, stage B is the initial fracture stage. However, in stage B, the number and energy proportions of the waveforms are both less than 10%. The main reason is that the coal body in stage B is under the comprehensive action of high-pressure water and three-dimensional pressure. Therefore, the internal compaction degree of the coal body is higher, and its integrity is good. When the water pressure reaches the peak value, the coal body was ruptured for the first time and formed a through crack. Moreover, the crack initiation speed is faster in stage B, so the waveform detected by AE is less than in other stages.

As shown in Figure 6(dI), the fraction with energy proportion less than 10% was enlarged. The number of the dominant frequency band waveform in Stage C to that in the whole HF process ratio is 26.79%, while its energy ratio is only 0.86%. The number proportion of the waveforms is 24.05% more than stage B, but the waveform energy is, at a minimum, 2.81% less than stage B. Generally speaking, the number of the waveform is positively correlated with the waveform energy. However, the proportion of the waveform number and energy in stage C is exactly the opposite. In stage C, the waveform energy to number ratio is the lowest in the whole process, which is 0.03. The AE waveform in stage C is characterized by the low energy and high frequency of the number. This indicates that, in stage C, the internal fracture form of the coal body is different from that of the other stages. Combined with the characteristics of the hydraulic pressure curve and window-number of the waveform, we analyzed the internal fracture form after the coal body first ruptured in stage B. As a result, the hydraulic pressure is immensely relieved, and the through crack is closed under the effect of three-dimensional pressure. At this time, the low-pressure water inside the coal body is not enough to maintain the original through crack. Therefore, the main reason is concluded that the coal body is mainly under the erosion weakening of low-pressure water in stage C. Moreover, the complex fracture mesh structure is formed on the through fracture surface path and extends to the end of the coal sample.

4.2. The Temporal Variation Characteristics of AE Waveforms' Amplitude and Cumulative Energy

Part of the energy released when the coal rupture occurred will spread in the form of elastic waves. The amplitude of the AE waveform can directly reflect the amount of energy released by coal failure. The maximum amplitude of the AE waveform in the HF process is picked up and normalized using a batch processing program. The normalized amplitude of the waveform is instantaneous. The cumulative energy is the sum of the waveform energy in time order. In order to highlight the change law at the early stage of loading, we used the Log10 coordinate system for the cumulative energy curve. The cumulative energy parameter reflects the changing trend of the waveform energy with the hydraulic pressure. Thus, we analyzed the time distribution characteristics of AE waveform amplitude and cumulative energy in the process of HF.

As shown in Figure 7, the waveform amplitude is small, and the cumulative energy curve does not rise significantly in stage A. There is a high-level response of amplitude in stage B, and the cumulative energy curve increased suddenly two times. Combined with

the significant pressure relief of the hydraulic pressure curve in stage B, we believe that the internal fracture scale of the coal body is large, and the released energy is more. The overall level of amplitude is low in stage C and early-stage D (1375–2049 s). As shown in Figure 7I, the cumulative energy curve presents a “trapezoidal” rise in the small area. The “trapezoidal” rise indicates that the scale of coal body fracture in this stage is tiny, and the amplitude and energy of the corresponding waveform are small. At 2094 s, the wave amplitude begins to change abruptly. The wave amplitude parameters have a higher overall level at the late period of stage D (2094–2399 s) and stage E (2399–2420 s). The cumulative energy curve increases gradually. The hydraulic pressure curve suddenly drops at 2339 s, which indicates that the coal failure in stage D. However, the form of fracture in the coal body is different from that in stage B. Therefore, we believe that the form of fracture propagation in this stage is more complicated than before.

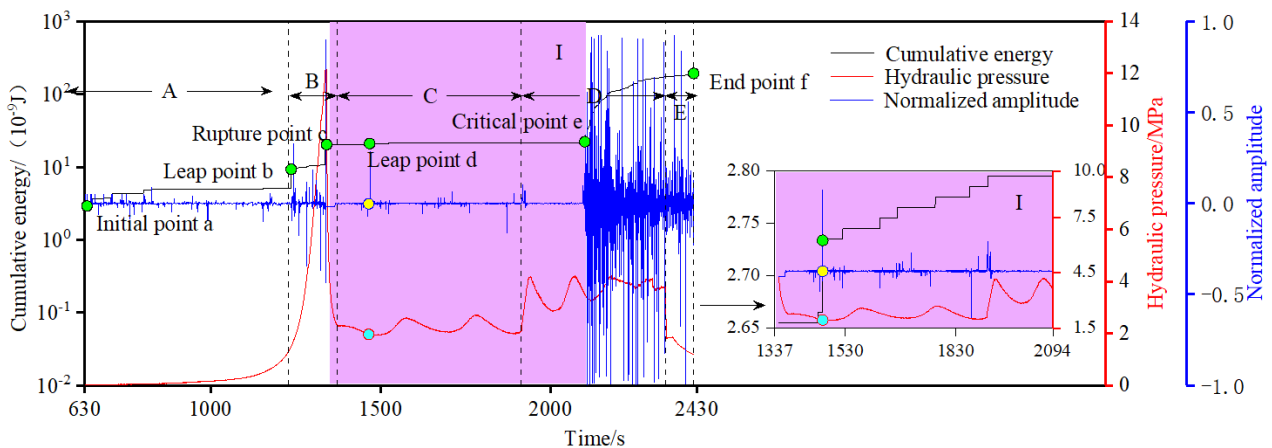


Figure 7. AE energy and normalized amplitude curve in true triaxial HF.

Combined with the distribution law of the normalized amplitude curve, we selected the key points of cumulative energy characteristics mutation in each stage. As shown in Figure 7, these points were marked respectively as initial point a, leap point b, rupture point c, leap point d, critical point e, and end point f.

The initial point a (630.8 s) is in stage A, and the normalized amplitude of this stage is low as a whole. The leap point b (1237.2 s) and the rupture point c (1340 s) are in stage B. The leap point b is in the process of hydraulic pressure rising sharply, and the rupture point c is at the peak of the hydraulic pressure. As shown in Figure 7I, the leap point d (1467.9 s) is in stage C. The normalized amplitude and cumulative energy curves are increased abruptly. The critical point e (2101.7 s) is in stage D. After the critical point e, the normalized amplitude curve and cumulative energy curve increase significantly. The end point f represents the end of the HF.

As shown in Figure 8, the amplitude diagrams of each key point are drawn respectively (the waveform length is set to 1000 μs). In Figure 8, t_{is} represents the arrival time of the waveform, and t_{im} represents the maximum amplitude time of the waveform, t_{io} represents the end time of waveform, t_i represents the duration of the waveform ($t = t_{is} - t_{io}$), and the waveform attenuation ratio indicator: $AT_i = (t_{io} - t_{im})/t_i$ (i is the key point serial number: a~f). When the waveform attenuation ratio is smaller, it means that the waveform attenuation rate is fast. Otherwise, it is slower. It can be seen from Table 4 for the amplitude, energy, and attenuation ratio parameters of each key point waveforms.

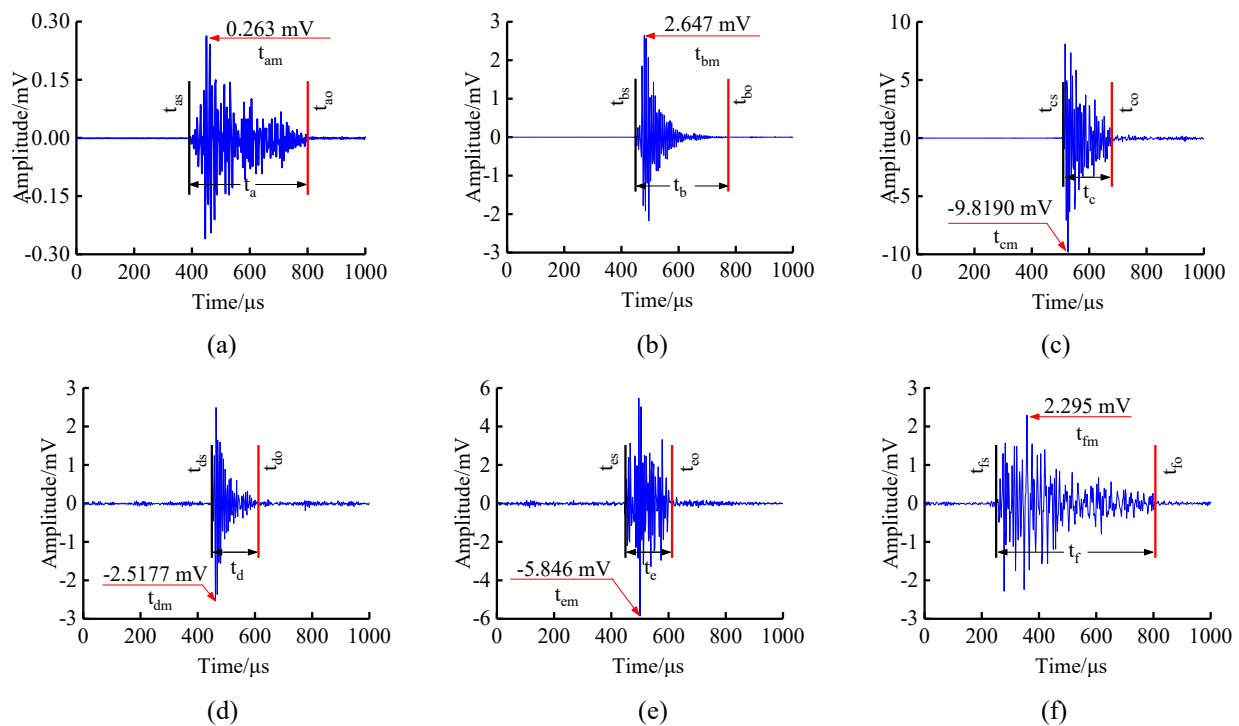


Figure 8. Amplitude diagram of key points in HF. (a) Initial point a, (b) Leap point b, (c) Rupture point c, (d) Leap point d, (e) Critical point e, and (f) End point f.

Table 4. Time–domain waveform parameters of the key points.

Key Points	Characteristics Parameters	Maximum Amplitude /mV	Energy/(10 ^{−9} J)	Attenuation Ratio
Initial point a		0.263	0.002	0.837
Leap point b		2.647	0.106	0.886
Rupture point c		−9.819	1.497	0.667
Leap point d		2.518	0.085	0.921
Critical point e		−5.846	0.586	0.658
End point f		2.295	0.177	0.772

As shown in Figure 9, the maximum amplitude waveform of the leap point b, the leap point d, and the end point f are averaged, and its value is 2.487 mV, and its variance is 0.03. In the same way, the mean value of wave energy is 0.123×10^{-9} J, and its variance is 0.03. It means that the wave maximum amplitude and energy fluctuation of these three points are relatively small. As shown in Figure 9I,II, the waveform amplitude and energy at rupture point c are the largest, and the amplitude and energy at critical point e are second to rupture point c. The maximum amplitudes of the rupture point c and the critical point e are 9.819 mV and 5.846 mV. Both maximum amplitudes are higher than that of the other key points. Meanwhile, the waveform energy of the rupture point c and the critical point e are 1.497×10^{-9} J and 0.586×10^{-9} J, respectively. The attenuation ratios of the rupture point C and the critical point E are 0.667 and 0.658, respectively, smaller than the other points. Obviously, the law of the waveform maximum amplitude and attenuation ratio of the two key points are opposite. It shows that, the larger the maximum amplitude of the waveform, the smaller the attenuation ratio. Furthermore, it means the shorter the post-peak phase of the waveform.

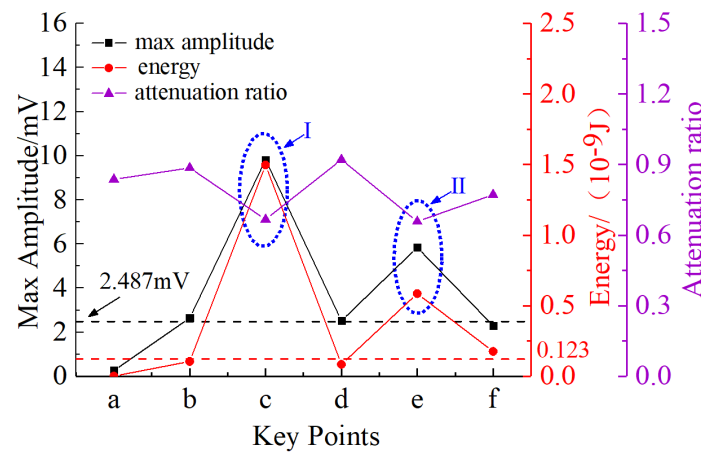


Figure 9. The characteristics of waveforms' time-domain parameters diagram of the key points.

4.3. The Window-Number Indicator of AE Waveform during True Triaxial HF Experiment

Based on the hydraulic pressure stages division, the waveform of the AE waveform parameters (dominant frequency, energy, amplitude, and cumulative energy) changes regularly in different stages. At the same time, we notice that the time distribution characteristics of the AE waveform parameters are quite different in different time intervals in a single stage. For example, in early-stage D (1915–2094 s), the response level of the AE waveform parameters is low, which is significantly different from that in late-stage D (2094–2399 s). Considering that coal is not only affected by water pressure and three-dimensional pressure but also eroded and weakened by water in the process of HF, the AE waveform is quite different.

As shown in Figure 10a, the maximum amplitude of the waveform is 9.6838 mV, and the ringing count of the waveform is 1487 times. The waveform energy is 4.6636×10^{-6} J, while, in Figure 10b, the maximum amplitude of the waveform is 0.0714 mV, the ringing count of the waveform is 1977 times, and the waveform energy is 4.9542×10^{-9} J. In contrast, Figure 10a is a unique waveform with low count and high amplitude, and Figure 10b is a unique waveform with high count and low amplitude. Here, we do not recommend the traditional ringing count and instantaneous energy indicator of AE waveform to characterize the internal damage degree and fracture propagation process of coal. These indicators are easy to be affected by a single unique waveform, like the two unique waveforms shown in Figure 10. Due to this, the accuracy and reliability of the indicator are reduced.

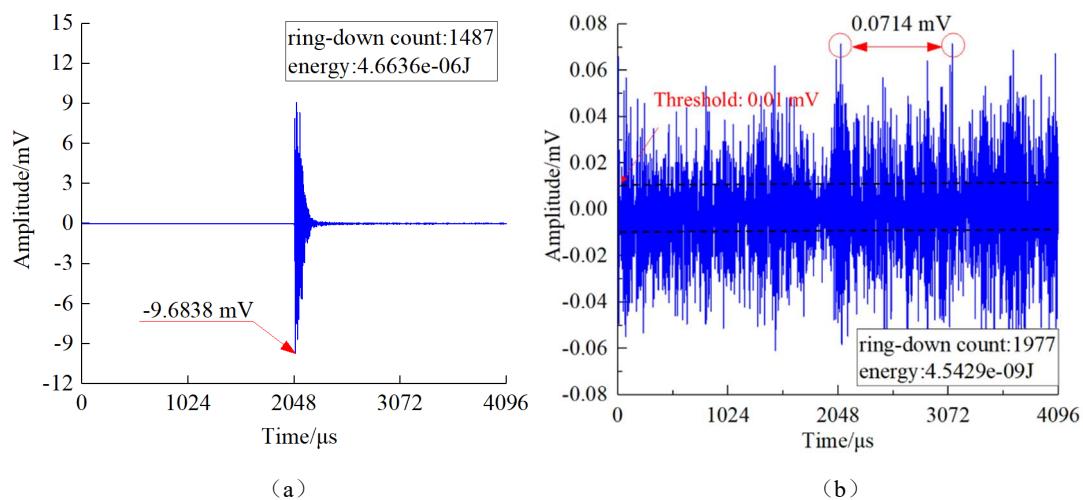


Figure 10. Two special waveforms in HF. (a) example waveform with low count and high amplitude: (b) example waveform with high count and low amplitude.

To address this issue, we put forward a unique monitoring and early warning indicator and named it as the window-number indicator, which is used to calculate the AE waveforms' numbers in the preset window. It can accurately reflect the degree of coal failure during HF. By contrast, the window-number indicator pays more attention to the numbers of the waveform in the unit window during HF but ignores the influence of the waveform parameters.

The statistical flow of the window-number indicator is as follows: firstly, according to the threshold value set in the AE monitoring test, we picked up the effective waveform of the AE monitoring waveform sequence during HF. Secondly, we divided the whole process according to the preset window. At last, we counted the number of effective AE waveforms in each window. For the convenience of operation, we ran the above steps through a batch program.

In this paper, the length of a window was defined as 0.5 s, the cumulative number of windows was 3580, since the whole time of the HF was 1790 s. Moreover, the batch program calculated the window-number indicator of the waveforms in a time order. The window-number indicator curve and hydraulic pressure curve of the whole process of HF are shown in Figure 11. It can be seen from Figure 11 that the window-number indicator of AE waveforms is mainly distributed in part of stages B, C, D, and E, and it presents a certain regularity in HF. At the same time, it can be found that there are differences in the distribution law of the window-number curve and the hydraulic pressure curve. Therefore, the window-number curve is reorganized into regions I~VI. Table 5 shows the basic information of the window-number indicator in these six regions.

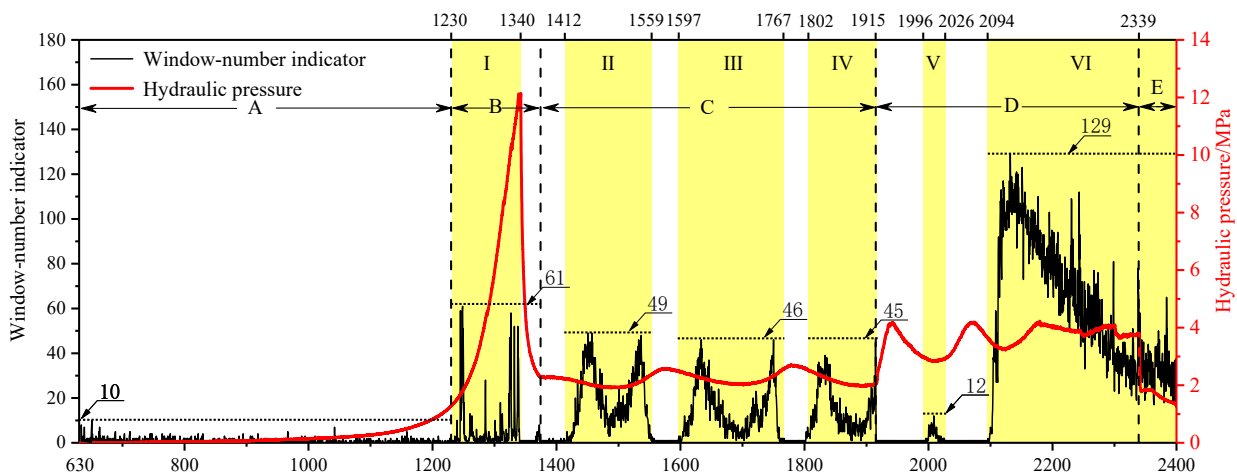


Figure 11. Hydraulic pressure and window-number indicator curve in HF.

Table 5. Window-number indicators in six regions (regions I~VI) during HF.

Regions	Stages	Time/s	Duration/s	Waveform Number	Maximum Window-Number Indicator	Mean Window-Number Indicator
I	B	1230–1340	110	1352	61	6
II	C	1412–1559	147	5556	49	19
III	C	1597–1767	170	4786	46	14
IV	C	1802–1915	113	3192	45	14
V	D	1996–2026	30	199	12	3
VI	D,E	2094–2420	326	37,958	129	58

In stage A, the maximum number of window-number indicator of the AE waveforms is 10, the mean window-number value is less than 1, and the overall response of AE waveform is at a low level.

Region I is in stage B, and its maximum window-number indicator is 61. It is higher near 1240 s and the peak hydraulic pressure (1340 s). We believe that the rupture occurred in the coal body.

Based on the time distribution characteristics of the AE waveform amplitude, there is a positive correlation between the window-number indicator curve and the AE waveform amplitude curve in region I. While the hydraulic pressure decreases instantaneously and the hydraulic pressure continues to rise, both the maximum amplitude and window-number indicator curves are kept at high levels. These characteristics prove that the fracture occurred in the coal body at this time. We concluded that the coal body around the bare hole section is affected by the hydraulic pressure, and the local crack occurred. The new fracture will expand the bare hole section confined cavity, resulting in the short-term decrease of the hydraulic pressure curve. As the water injection rate remains unchanged, the water will soon fill the whole cavity and hold the pressure again. Therefore, the hydraulic pressure will continue to rise after a short decrease. When the hydraulic pressure reaches the peak value, the bare hole section cavity of the coal body is damaged, the fracture penetrating through the coal sample, the water flows out of the coal body along the fracture path, and the hydraulic pressure is greatly relieved.

Regions II, III, and IV are all in stage C. With the fluctuation of the hydraulic pressure curve, the window-number indicator of AE waveform increased and decreased regularly. The maximum window-number indicator is 49 in stage C, which is lower than that in stage B. Moreover, in these regions, the correlation between the window-number indicator curve and the AE waveforms' amplitude curve is different from that in region I. The overall level of maximum amplitude of the AE waveform is generally low in stage C. All of this shows that there are many low amplitude waveforms in this stage. Thus, we believe that the internal crack of the coal body in this stage is small. We concluded that the fracture form during the liquid storage space expansion stage was different from that in region I. In stage C, water erosion played a leading role in weakening the coal body. Under the three-dimensional pressure and the low overall level of the hydraulic pressure, the liquid storage space in the coal body gradually expands from the bare hole section to the coal sample surface along the initial crack initiation path.

Region V belongs to early-stage D (1915–2094 s), and the maximum window-number indicator is 12, which is the minimum in the six regions. Combined with the AE amplitude parameter characteristics, we concluded that, under the action of high-pressure water, the cavity in the coal body expands to the initial fracture surface. After high-pressure water fills the whole cavity, the water pressure begins to hold, and no AE signal is generated during this process. When the water pressure exceeds the minimum principal stress 4 MPa, the cracks are connected. Moreover, the water flows out of the coal body, causing the hydraulic pressure to decrease. There is no AE signal during the water flow process. When the hydraulic pressure decreases to the critical value, under the action of three-dimensional pressure, the fracture end face closes again. The AE signal is generated when the coal body is compressed. When the water pressure starts to hold again, there is little waveform signal in this process.

Region VI consists of late-stage D (2094–2399 s) and the whole of stage E. The window-number indicator of the waveforms first increases and then decreases, and the maximum window-number indicator is 129, which is the maximum of the six regions. It is the opposite of region V. All of this indicates that the fracture forms in the coal body between region V and region VI are different. Similarly, combined with the hydraulic pressure characteristics, a positive correlation exists between the window-number indicator curve and the AE waveform amplitude curve in region VI. We concluded that water filled the initial through crack after changing the water injection rate from 100 ml/min to 200 ml/min. Due to the weakening effect of water on coal, the initial crack end continues to expand until the coal is destroyed. The hydraulic pressure and three-dimensional pressure reach a dynamic balance, with the water flowing out from the coal regularly.

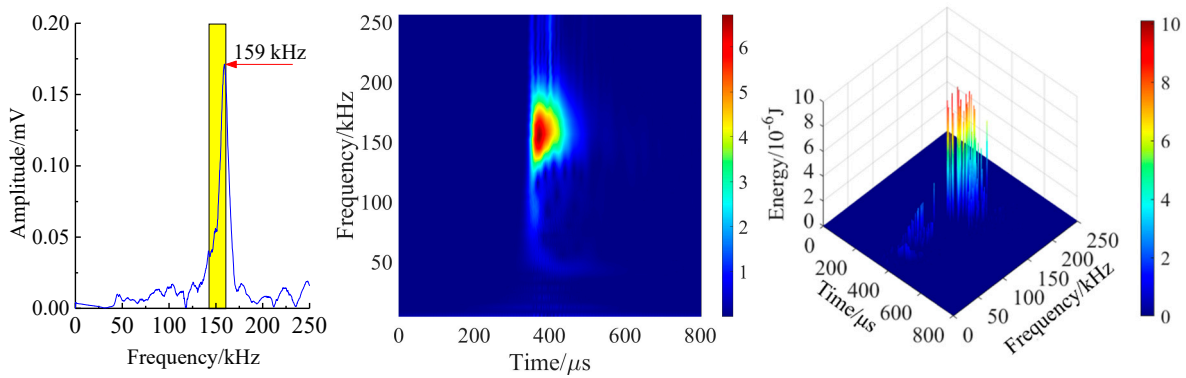
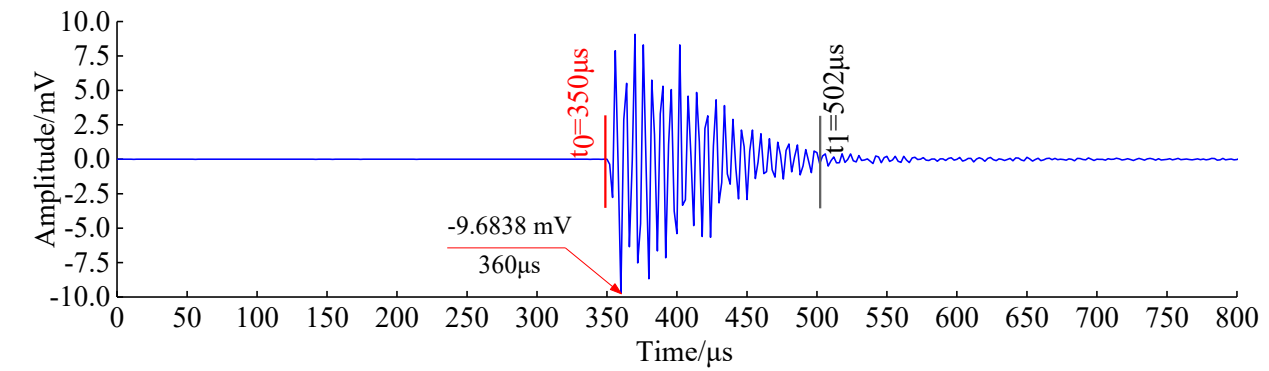
5. Discussion

In Section 4.3, it is concluded that the two types of special waveforms will have a great impact on the accuracy of traditional indicators by analyzing the time–domain characteristics parameters of two waveforms shown in Figure 10, such as the AE energy and ring-down count. This section presents a time–frequency analysis on the two waveforms as shown in Figure 10 by using the FFT, wavelet transform, and HHT methods [67].

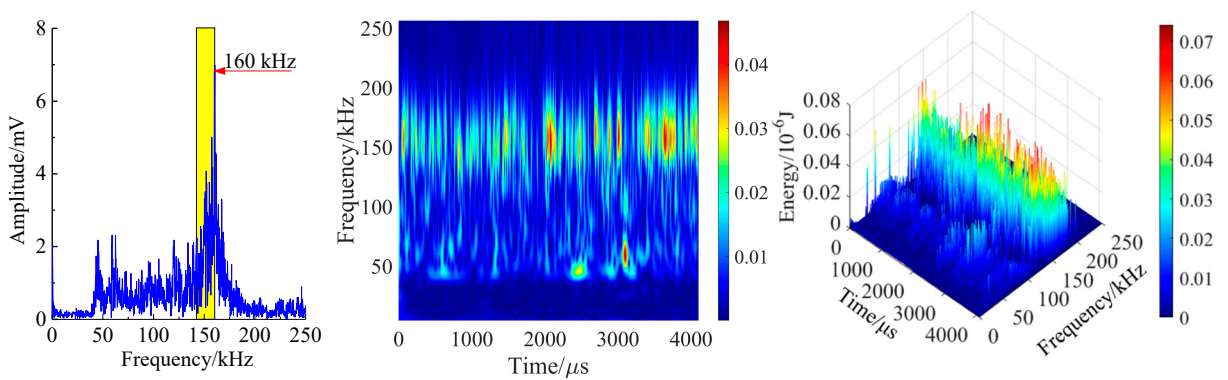
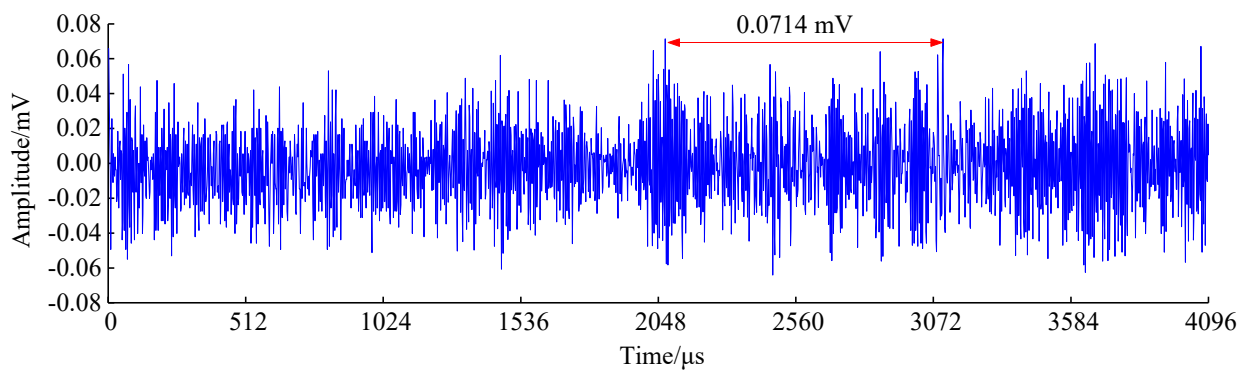
As shown in Figure 12, waveform HW1 is selected from point P1 in Figure 4, and the SNR of waveform HW1 is high at the initial rupture of HF. Waveform HW2 is selected from the liquid storage space expansion stage (stage C), and its SNR is low. As shown in Figure 12a, the maximum magnitude of waveform HW1 is 9.6838 mV, the maximum magnitude time is 360 μ s, the waveform arrival time t_0 is 350 μ s, the waveform end time t_1 is 502 μ s, the waveform duration is 152 μ s, and the waveform decay ratio is 93.4%. As shown in Figure 12b, the maximum amplitude of the waveform HW2 is 0.0714 mV. Obviously, in the time window of 4098 μ s, there are two points in this waveform with an amplitude of 0.0714 mV. In addition, the waveform has no apparent arrival time and end time.

Comparing the amplitude–frequency plots of the two waveforms, we can see that the dominant frequency of both waveforms HW1 and HW2 are distributed in the dominant frequency band. The range of the dominant frequency band is the yellow area in the Figure 12. Among them, the dominant frequency of waveform HW1 is 159 kHz, and the dominant frequency of waveform HW2 is 160 kHz. From the time–frequency diagram of the two waveforms, waveform HW2 is a typical broadband signal, and the frequency range of waveform HW2 is more extensive than that of waveform HW1. In the duration, the dominant frequency distribution of waveform HW1 is concentrated. The peak energy is around 150 kHz, while the frequency distribution in background noise is discrete, and the corresponding energy is small. The energy distribution of waveform HW2 is discrete in the time series and frequency band. Observing the three-dimensional spectra of the two waveforms, their time–frequency distribution characteristics and wavelet transform characteristics are the same. However, waveform HW2 contains more low-frequency components, and the spectrum of waveform HW2 is more complex than that of HW1.

Combined with the division of HF stages and the time–frequency characteristics of AE waveform, we draw the following conclusions: the waveform HW1 is the waveform generated by initial rupture (the initial rupture stage), with a high amplitude, concentrated frequency, and narrow frequency band. The waveform HW2 is a unique waveform that frequently appears after the initial through rupture has occurred (the liquid storage space expansion stage). It has a low amplitude, multipeak, no apparent duration, wide frequency band, more low-frequency components, and complex frequency spectrum. At the same time, we found a large number of waveforms similar to waveform HW2 in stage C. In addition, we found that there is a negative correlation between the proportion of wave number and energy in stage C. The waveforms' number proportions in stage C are second only to stage B, while the energy proportion is the least. From the analysis of the waveforms' amplitudes, we found that the overall level of amplitude was low in stage C. All of these showed that waveform HW2 is a special type of waveform in the HF, not a special case. Combined with the characteristics of the window-number indicator in stage C, we inferred that this kind of waveform is a mixed waveform. We guess that this waveform was generated by the repeated erosion and weakening of the initial through crack by water with a lower pressure.



(a)



(b)

Figure 12. Time frequency diagram of two AE waveforms corresponds to FFT, WT and HHT. (a): HW1; (b): HW2.

6. Conclusions

We developed a true triaxial HF experiment system for coal and rock. Under the true triaxial stress, we carried out a hydraulic fracturing experiment of coal samples combined with AE monitoring. Moreover, we programmed the traditional time–frequency methods and design batch programs for picking the AE waveform parameters, such as the dominant frequency, energy, maximum amplitude, and cumulative energy. Based on this, the injection pressure curves and temporal variations of the AE waveforms' parameters in different stages were analyzed in detail. The relationship between the characteristics of the AE waveforms' parameters and the propagation and evolution regularity of the hydraulic fracture in coal were further qualitatively discussed. The main conclusions are as follows:

(1) We found that there are two strong fracture behaviors in the coal body during the HF, resulting in a decreasing water pressure. After the initial fracture, the water pressure decreases sharply from 12.157 MPa to 2.230 MPa and keeps rising and falling dynamically at the low level of 2.230 MPa. After the water injection rate changes from 100 mL/min to 200 mL/min, the water pressure curve increases. Eventually, the water pressure decreases a second time. The effect of water pressure relief caused by the secondary fracture is far smaller than that of the first fracture. Therefore, according to the phenomena of the true triaxial HF experiment and the variation characteristics of the hydraulic pressure curve of the coal samples, the HF process of coal samples can be divided into five stages.

(2) The distribution range of the AE waveform is 30–270 kHz, of which the majority of the dominant frequency is distributed between 145 and 160 kHz, and the waveform number in this frequency band to the whole frequency band ratio is up to 83.97%, and the proportion of its energy is up to 87.28%. Moreover, the number and energy proportions of these frequency band waveforms in each stage of HF are more than 65.00%. This frequency band is defined as the dominant frequency band of the whole band. The number proportion of the dominant frequency band waveform in each stage to that in the whole HF process ratio generally increases first and then decreases and reaches the maximum value of 61.49% in stage D. Similarly, the energy proportion in stage D accounts for 87.60%, and its proportion in other stages is less than 10.00%. Moreover, there is a negative correlation between the proportion of the wave number and energy in stage C, which indicates that the internal fracture form of the coal body in stage C is different from that of the other stages.

(3) The amplitude of the AE waveform can directly reflect the amount of energy released by a rupture. The normalized amplitude of the waveform is instantaneous, and the cumulative energy parameter reflects the changing trend of the waveform energy with the hydraulic pressure. The waveform amplitude is small, and the cumulative energy curve does not rise significantly in stage A. There are high-level responses of the amplitude in stage B, the late period of stage D (2094–2399 s), and stage E (2399–2420 s) for the amplitude curve of the AE waveform. For the cumulative energy curve, it increases suddenly two times in stage B. It presents a “trapezoidal” rise in the small area of stage C and early-stage D (1375–2049 s), indicating that the scale of the coal body fracture in this stage is tiny, and the amplitude and energy of the corresponding waveform are small. The cumulative energy curve gradually increases in the late period of stage D (2094–2399 s) and stage E (2399–2420 s). It indicates that the form of the fracture in the coal body in stage D is different from that in stage B, and the form of the fracture propagation in this stage is more complex than before.

(4) We put forward a monitoring and early warning indicator: the window-number indicator of the AE waveform to reflect the degree of coal failure during HF accurately, and it can optimize the stage division of the HF. The traditional ringing count and instantaneous energy indicator are easily affected by a single unique waveform or even self-contradiction, which reduces the accuracy and reliability of the indicator. By contrast, the window-number indicator pays more attention to the number of the waveform in the unit window during HF but ignores the influence of the waveform parameters, such as ringing count and instantaneous energy. The window-number indicator of the AE waveforms is mainly distributed in stages B, C, D, and E, presenting a certain regularity in HF. It can be found that

there are differences in the distribution law of the window-number curve and the hydraulic pressure curve. Therefore, the window-number curve is reorganized into regions I–VI. Regions II, III, and IV are all in stage C. With the fluctuation of the hydraulic pressure curve, the window-number indicator of the AE waveform increased and decreased regularly. There is a negative correlation between the window-number indicator curve and the AE waveform amplitude curve. The overall level of the maximum amplitude of the AE waveform is generally low in stage C. All of this shows that there are many low-amplitude waveforms in this stage, which indicates that the internal crack of the coal body in this stage is small. It confirmed that the fracture form during stage C is different from that in stage B. Moreover, the window-number indicator distribution characteristics are different between early-stage D and late-stage D. Therefore, the window-number indicator can optimize the division of the HF process and improve the understanding of the internal fracture behavior and fracture form of coal in each stage.

Author Contributions: Conceptualization, N.L., L.F., B.H., P.C. and C.C.; methodology, N.L., L.F., P.C., C.C., Y.W. and Y.Q.; formal analysis, N.L., L.F., P.C., C.C., Y.Z., X.L. and Z.L.; investigation, N.L. and B.H.; resources, N.L., L.F. and B.H.; data curation, N.L., L.F. and P.C.; writing—original draft preparation, N.L., L.F. and P.C.; writing—review and editing, N.L. and L.F.; supervision, N.L., L.F. and B.H.; funding acquisition, N.L. and L.F. All authors have read and agreed to the published version of the manuscript.

Funding: This work was funded by the Natural Science Foundation of Jiangsu Province (BK20190080), the National Natural Science Foundation of China (52174221 and 51874296), the China Postdoctoral Science Foundation Grant (2018M640533), and the Postgraduate Research & Practice Innovation Program of Jiangsu Province (KYCX21_2344).

Institutional Review Board Statement: Not applicable.

Informed Consent Statement: Not applicable.

Data Availability Statement: Not applicable.

Acknowledgments: We would like to thank the editor and anonymous reviewers for their constructive comments. We would like to thank Xin Zhang from the University of New South Wales for his help in doing the laboratory experiments.

Conflicts of Interest: The authors declare no conflict of interest.

Glossary

t_{is}	arrival time of the waveform, s
t_{io}	end time of the waveform, s
t_{im}	maximum amplitude time of the waveform, s
t_i	duration time of the waveform, s
AT_i	attenuation ratio indicator

References

1. Economides, M.; Martin, T. *Modern Fracturing: Enhancing Natural Gas Production*; Energy Tribune Publishing Inc.: Houston, TX, USA, 2007.
2. Tang, Y.; Tang, X.; Wang, G.Y.; Zhang, Q. Summary of hydraulic fracturing technology in shale gas development. *Geol. Bull. China* **2011**, *30*, 393–399.
3. Hou, M.X.; Ge, X.R.; Wang, S.L. Discussion on application of hydraulic fracturing method to geostress measurement. *Rock Soil Mech.* **2003**, *24*, 840–844.
4. Huang, B.X. *Hydraulic Fracturing Theory of Coal-Rock Mass and Its Application*; China University of Mining and Technology Press: Xuzhou, China, 2012.
5. Wang, Y.F.; He, X.Q.; Wang, E.Y.; Li, Y.Z. Research progress and development tendency of the hydraulic technology for increasing the permeability of coal seams. *J. China Coal Soc.* **2014**, *39*, 1945–1955.
6. Kang, H.P.; Feng, Y.J. Monitoring of stress change in coal seam caused by directional hydraulic fracturing in working face with strong roof and its evolution. *J. China Soc.* **2012**, *37*, 1953–1959.

7. Hardy, R. *Acoustic Emission/Microseismic Activity: Volume 1: Principles, Techniques and Geotechnical Application*; A.A. Balkema Publishers: De Wallen, Amsterdam, 2003.
8. Li, N.; Wang, E.Y.; Ge, M.C. Microseismic monitoring technique and its applications at coal mines: Present status and future prospects. *J. China Coal Soc.* **2017**, *42*, 83–96.
9. Ishida, T.; Labuz, J.F.; Manthei, G.; Meredith, P.G.; Nasser, M.H.B.; Shin, K.; Yokoyama, T.; Zang, A. ISRM Suggested method for laboratory acoustic emission monitoring. *Rock Mech. Rock Eng.* **2017**, *50*, 665–674. [[CrossRef](#)]
10. Jiang, R.C.; Dai, F.; Liu, Y.; Li, A.; Feng, P. Frequency characteristics of acoustic emissions induced by crack propagation in rock tensile fracture. *Rock Mech. Rock Eng.* **2021**, *54*, 2054–2065. [[CrossRef](#)]
11. Petružálek, M.; Lokajíček, T.; Svitek, T.; Jechumtálová, Z.; Kolář, P.; Šílený, J. Fracturing of migmatite monitored by acoustic emission and ultrasonic sounding. *Rock Mech. Rock Eng.* **2019**, *52*, 47–59. [[CrossRef](#)]
12. He, M.C.; Miao, J.L.; Feng, J.L. Rock burst process of limestone and its acoustic emission characteristics under true-triaxial unloading conditions. *Int. J. Rock Mech. Mining Sci.* **2010**, *47*, 286–298. [[CrossRef](#)]
13. Lei, X.L.; Kusunose, K.; Rao, M.V.M.S.; Nishizawa, O.; Satoh, T. Quasi-static fault growth and cracking in homogeneous brittle rock under triaxial compression using acoustic emission monitoring. *J. Geophys. Res.* **2000**, *105*, 6127–6139. [[CrossRef](#)]
14. Meng, Q.B.; Zhang, M.W.; Han, L.J.; Pu, H.; Chen, Y.L. Acoustic emission characteristics of red sandstone specimens under uniaxial cyclic loading and unloading compression. *Rock Mech. Rock Eng.* **2018**, *51*, 969–988. [[CrossRef](#)]
15. Li, D.X.; Wang, E.Y.; Kong, X.G.; Ali, M.; Wang, D.M. Mechanical behaviors and acoustic emission fractal characteristics of coal specimens with a pre-existing flaw of various inclinations under uniaxial compression. *Int. J. Rock Mech. Min. Sci.* **2019**, *116*, 38–51. [[CrossRef](#)]
16. Du, K.; Li, X.F.; Tao, M.; Wang, S.F. Experimental study on acoustic emission (AE) characteristics and crack classification during rock fracture in several basic lab tests. *Int. J. Rock Mech. Min. Sci.* **2020**, *133*, 104411. [[CrossRef](#)]
17. Zhang, R.; Xie, H.P.; Liu, J.F.; Deng, J.H.; Peng, Q. Experimental study on acoustic emission characteristics of rock failure under uniaxial multilevel loadings. *Chin. J. Rock Mech. Eng.* **2006**, *25*, 2584–2588.
18. Zhao, X.D.; Li, Y.H.; Liu, J.P.; Zhang, J.Y.; Zhu, W.C. Study on rock failure process based on acoustic emission and its location technique. *Chin. J. Rock Mech. Eng.* **2008**, *27*, 990–995.
19. Li, N.; Wang, E.Y.; Zhao, E.L.; Ma, Y.K.; Xu, F.L.; Qian, W.H. Experiment on acoustic emission of rock damage and fracture under cyclic loading and multi-stage loading. *J. China Coal Soc.* **2010**, *35*, 1099–1103.
20. Liu, S.M.; Li, X.L.; Li, Z.H.; Chen, P.; Yang, X.L.; Liu, Y.J. Energy distribution and fractal characterization of acoustic emission (AE) during coal deformation and fracturing. *Measurement* **2019**, *136*, 122–131. [[CrossRef](#)]
21. Li, J.; Yue, J.H.; Yang, Y.; Zhan, X.Z.; Li, Z. Multi-Resolution Feature Fusion model for coal rock burst hazard recognition based on Acoustic Emission data. *Measurement* **2017**, *100*, 329–336. [[CrossRef](#)]
22. Li, H.R.; Yang, C.H.; Li, B.L.; Yin, X.Y. Damage evolution and characteristics of ultrasonic velocity and acoustic emission for salt rock under triaxial multilevel loading test. *Chin. J. Rock Mech. Eng.* **2016**, *35*, 682–691.
23. Wu, S.C.; Huang, X.Q.; Chen, F.; Chai, J.F.; Wu, H.Y. Moment tensor inversion of rock failure and its application. *Rock Soil Mech.* **2016**, *37*, 1–18.
24. Petružálek, M.; Jechumtálová, Z.; Kolář, P.; Adamová, P.; Svitek, T.; Šílený, J.; Lokajíček, T. Acoustic Emission in a Laboratory: Mechanism of Microearthquakes Using Alternative Source Models. *J. Geophys. Res. Solid Earth* **2018**, *123*, 4965–4982. [[CrossRef](#)]
25. Li, S.L.; Zhou, M.J.; Gao, Z.P.; Chen, D.X.; Zhang, J.L.; Hu, J.Y. Experimental study on acoustic emission characteristics before the peak strength of rocks under incrementally cyclic loading-unloading methods. *Chin. J. Rock Mech. Eng.* **2019**, *38*, 724–735.
26. Wang, X.R.; Li, N.; Wang, E.Y.; Liu, X.F. Microcracking mechanisms of sandstone from acoustic emission source inversion. *Chin. J. Geophys.* **2020**, *63*, 2627–2643.
27. Wang, C.Y.; Chang, X.K.; Du, X.Y. Analysis on Dominant-frequency Characteristics of Acoustic Emission in Sandstone Uniaxial Compression Failure. *Chin. J. Undergr. Space Eng.* **2020**, *16*, 451–462.
28. Wang, C.Y.; Chang, X.K.; Liu, Y.L.; Guo, W.B. Spectrum evolution characteristics of acoustic emission during the rupture process of marble under uniaxial compression condition. *Rock Soil Mech.* **2020**, *41*, 51–62.
29. Zeng P.Liu, Y.J.; Ji, H.G.; Li, C.J. Coupling criteria and precursor identification characteristics of multi-band acoustic emission of gritstone fracture under uniaxial compression. *Chin. J. Geotech. Eng.* **2017**, *39*, 509–517.
30. Wang, Q.; Zhou, Y.Y.; Li, Y.H.; Zhang, F.P. Experimental study on deformation and strength characteristics of diabase containing natural weak plane by acoustic emission. *Chin. J. Rock Mech. Eng.* **2019**, *38*, 3646–3653.
31. Zhang, Y.B.; Liang, P.; Tian, B.Z.; Yao, X.L.; Sun, L.; Liu, X.X. Multi parameter coupling analysis of acoustic emission signals of granite disaster and the precursor characteristics of the main rupture. *Chin. J. Rock Mech. Eng.* **2016**, *35*, 2248–2258.
32. Ji, H.G.; Lu, X. Characteristics of acoustic emission and rock fracture precursors of granite under conventional triaxial compression. *Chin. J. Rock Mech. Eng.* **2015**, *34*, 2248–2258.
33. Zhang, Y.B.; Zhang, H.; Liang, P.; Chen, S.J.; Sun, L.; Yao, X.L.; Liu, X.X.; Liang, J.L. Experimental research on time-frequency characteristics of AE P-wave and S-wave of granite under failure process. *Chin. J. Rock Mech. Eng.* **2019**, *38*, 3554–3564.
34. Yang, Y.J.; Ma, D.P.; Zhou, Y. Experimental research on spectrum signature eigen of acoustic emission of coal and sandstone damage under triaxial unloading confining pressure. *J. Min. Saf. Eng.* **2019**, *36*, 1002–1008.
35. Zhang, L.M.; Wang, Z.Q.; Shi, L.; Kong, L. Acoustic emission characteristics of marble during failure process under different stress paths. *Chin. J. Rock Mech. Eng.* **2012**, *31*, 1230–1236.

36. Zhang, N.B.; Qi, Q.X.; OuYang, Z.H.; Li, H.Y.; Zhao, S.K.; Xu, Z.J. Experimental on acoustic emission characteristics of marble with different stress paths. *J. China Coal Society* **2014**, *39*, 389–394.
37. Pei, X.J.; Zhu, L.; Cui, S.H.; Liang, Y.F. Experimental study on acoustic emission characteristic of rocks with vein mass. *Chin. J. Rock Mech. Eng.* **2020**, *39*, 2602–2611.
38. Li, Z.L.; He, X.Q.; Dou, L.M.; Wang, G.F.; Song, D.Z.; Lou, Q. Bursting failure behavior of coal and response of acoustic and electromagnetic emissions. *Chin. J. Rock Mech. Eng.* **2019**, *38*, 2057–2068.
39. Zhang, Y.B.; Yu, G.Y.; Tian, B.Z.; Liu, X.X.; Liang, P.; Wang, Y.D. Experimental study of acoustic emission signal dominant-frequency characteristics of rockburst in a granite tunnel. *Rock Soil Mech.* **2017**, *38*, 1258–1266.
40. Hou, B.; Chen, M.; Tan, P.; Li, D.D. Monitoring of hydraulic fracture network by acoustic emission method in simulated tri-axial fracturing system of shale gas reservoirs. *J. China Univ. Pet.* **2015**, *39*, 66–71.
41. Chong, Z.H.; Li, X.H.; Hou, P.; Chen, X.Y.; Wu, Y.C. Moment tensor analysis of transversely isotropic shale based on the discrete element method. *Int. J. Min. Sci. Technol.* **2017**, *27*, 507–515. [[CrossRef](#)]
42. Patel, S.M.; Sondergeld, C.H.; Rai, C.S. Laboratory studies of hydraulic fracturing by cyclic injection. *Int. J. Rock Mech. Min. Sci.* **2017**, *95*, 8–15. [[CrossRef](#)]
43. Ishida, T.; Fujito, W.; Yamashita, H.; Naoi, M.; Fujii, H.; Suzuki, K.; Matsui, H. Crack Expansion and Fracturing Mode of Hydraulic Refracturing from Acoustic Emission Monitoring in a Small-Scale Field Experiment. *Rock Mech. Rock Eng.* **2019**, *52*, 543–553. [[CrossRef](#)]
44. Fan, M.; Jin, Y.; Fu, W.N.; Chen, M.; Han, H.F.; Zhou, X.J. Experimental study on fracture propagation behavior based on acoustic emission characteristics. *Chin. J. Rock Mech. Eng.* **2018**, *37*, 3834–3841.
45. Hampton, J.; Gutierrez, M.; Matzar, L.; Hu, D.D.; Frash, L. Acoustic emission characterization of microcracking in laboratory-scale hydraulic fracturing tests. *J. Rock Mech. Geotech. Eng.* **2018**, *10*, 805–817. [[CrossRef](#)]
46. Naoi, M.; Chen, Y.; Nishihara, K.; Yamamoto, K.; Yano, S.; Watanabe, S.; Morishige, Y.; Kawakata, H.; Akai, T.; Kurosawa, I.; et al. Monitoring hydraulically-induced fractures in the laboratory using acoustic emissions and the fluorescent method. *Int. J. Rock Mech. Min. Sci.* **2018**, *104*, 53–63. [[CrossRef](#)]
47. Gao, L.; Gao, F.; Zhang, Z.Z.; Xing, Y. Research on the energy evolution characteristics and the failure intensity of rocks. *Int. J. Min. Sci. Technol.* **2020**, *30*, 705–713. [[CrossRef](#)]
48. Zhao, Z.J.; Liu, D.A.; Cui, Z.D.; Tang, T.W.; Han, W.G. Cyclic progressive pressure on the fracturing effect of shale. *Chin. J. Rock Mech. Eng.* **2019**, *38*, 2779–2789.
49. Hu, L.B.; Ghassemi, A.; Pritchett, J.; Garg, S. Characterization of laboratory-scale hydraulic fracturing for EGS. *Geothermics* **2020**, *83*, 101706. [[CrossRef](#)]
50. Li, N.; Zhang, S.; Zou, Y.; Ma, X.; Zhang, Z.; Li, S.; Chen, M.; Sun, Y. Acoustic Emission Response of Laboratory Hydraulic Fracturing in Layered Shale. *Rock Mech. Rock Eng.* **2018**, *51*, 3395–3406. [[CrossRef](#)]
51. Bingxiang, H. Research on Theory and Application of Hydraulic Fracture Weakening For Coal-Rock Mass. *J. China Coal Soc.* **2010**, *35*, 1765–1766.
52. Ding, H. Law of Hydraulic Fracturing Crack Initiation in the Multi-layered Coal Seams. *MA Diss. Chongqing Univ.* **2014**.
53. Jiang, Y.L.; Liang, W.G.; Li, Z.G.; Lian, H.J.; Wu, P.F.; Geng, Y.D. Experimental study on fracturing across coal-rock interfaces and the acoustic emission response characteristics. *Chin. J. Rock Mech. Eng.* **2019**, *38*, 875–887.
54. Li, N.; Sun, W.C.; Huang, B.X.; Chen, D.; Zhang, S.H.; Yan, M.Y. Acoustic emission source location monitoring of laboratory-scale hydraulic fracturing of coal under true triaxial stress. *Nat. Resour. Res.* **2021**, *30*, 2297–2315. [[CrossRef](#)]
55. Zhang, Y.B.; Liang, P.; Sun, L.; Tian, B.Z.; Yao, X.L.; Liu, X.X. Spectral characteristics of AE in the process of saturated granite fracture under uniaxial compression. *Rock Soil Mech.* **2019**, *40*, 2497–2506.
56. He, M.C.; Zhao, F.; Zhang, Y.; Du, S.; Guan, L. Feature evolution of dominant frequency components in acoustic emissions of instantaneous strain-type granitic rockburst simulation tests. *Rock Soil Mech.* **2015**, *36*, 1–8,33.
57. Pu, X.J.; Wen, J.F.; Lin, R.R.; Wang, Y.Q.; Zhang, L.Q. *Long-Term Monitoring Plan for Potential Magma Reservoir and Microseismic Observation of Datun Volcano Group*; China Geophysics Society: Taiwan, China, 2006.
58. Li, N.; Huang, B.X.; Zhang, X.; Tan, Y.Y.; Li, B.L. Characteristics of microseismic waveforms induced by hydraulic fracturing in coal seam for coal rock dynamic disasters prevention. *Saf. Sci.* **2019**, *115*, 188–198. [[CrossRef](#)]
59. Li, N.; Li, B.; Chen, D.; Wang, E.; Tan, Y.; Qian, J.; Jia, H. Waveform Characteristics of Earthquakes Induced by Hydraulic Fracturing and Mining Activities: Comparison with Those of Natural Earthquakes. *Nat. Resour. Res.* **2020**, *29*, 3653–3674. [[CrossRef](#)]
60. Tang, J.P.; Lu, J.W.; Xu, P.; Ding, J.H.; Qi, T. Experimental study on time-frequency characteristics of hydraulic fracturing acoustic emission in coal shale. *China Saf. Sci. J.* **2017**, *27*, 87–92.
61. Liang, T.C.; Fu, H.F.; Liu, Y.Z.; Xiu, N.L.; Yan, Y.Z. On the determination method of rupture mechanism in acoustic emission used in hydraulic fracturing fracture propagation. *J. Exp. Mech.* **2019**, *34*, 358–364.
62. Niu, Y.; Zhou, X.P.; Berto, F. Temporal dominant frequency evolution characteristics during the fracture process of flawed red sandstone. *Theor. Appl. Fract. Mech.* **2020**, *110*, 102838. [[CrossRef](#)]
63. Li, B.L.; Li, N.; Wang, E.Y.; Li, X.L.; Niu, Y.; Zhang, X. Characteristics of coal mining microseismic and blasting signals at Qianqiu coal mine. *Environ. Earth Sci.* **2017**, *76*, 722. [[CrossRef](#)]

64. Wang, C.Y.; Chang, X.K.; Liu, Y.L.; Chen, S.J. Mechanistic characteristics of double dominant frequencies of acoustic emission signals in the entire fracture process of fine sandstone. *Energies* **2019**, *12*, 3959. [[CrossRef](#)]
65. Li, B.L.; Li, N.; Wang, E.Y.; Li, X.L.; Zhang, Z.B.; Zhang, X.; Niu, Y. Discriminant model of coal mining microseismic and blasting signals based on waveform characteristics. *Shock. Vib. Deep. Min. Sci.* **2017**, *2017*, 6059239. [[CrossRef](#)]
66. Jia, X.N. *Experimental Study on Acoustic Emission Eigen-Frequency Spectrum Features of Strain Bursts*; University of Mining and Technology: Beijing, China, 2013.
67. Torres, M.E.; Colominas, M.A.; Schlotthauer, G.; Flandrin, P. A complete Ensemble Empirical Mode decomposition with adaptive noise. In Proceedings of the IEEE International Conference on Acoustics, Speech and Signal Processing (ICASSP), Prague, Czech Republic, 22–27 May 2011; pp. 4144–4147.